Editors' Suggestion

Tailoring spin-exchange interactions and topological magnons in 2D ferromagnetic van der Waals CrI_3/As bilayer via multiple stacking orders: A first-principles study

Andi Gumarilang* and Kohji Nakamura
Graduate School of Engineering, Mie University, Mie 514-8507, Japan

(Received 31 October 2025; accepted 27 January 2026; published 17 February 2026; corrected 16 March 2026)

Discovery of two-dimensional ferromagnetic van der Waals chromium triiodide (CrI_3) opens new avenues toward tunable terahertz topological magnon via stacking order control in a multilayer system. We theoretically simulated magnetism and topological magnon modulation in multiple CrI_3/As stacking orders by means of first-principles and linear spin-wave theory calculations. The first-nearest-neighbor spin-exchange interactions are enhanced up to 100% from those in monolayer CrI_3 due to degeneracy lifting in Cr *d* orbitals induced by broken symmetry from the addition of As monolayer. Furthermore, interfacial charge transfer from the As monolayer to I atom in the bottom sublayer induces finite Dzyaloshinskii-Moriya interactions of first-nearest-neighboring Cr atoms and enhances those of second-nearest-neighboring Cr atoms. Magnon Dirac gaps in bilayer CrI_3/As are open wider than those in monolayer CrI_3 at the edge of the Brillouin zone, attributed to the enhanced second-nearest-neighbor Dzyaloshinskii-Moriya interactions. The magnon dispersion in a nanoribbon geometry exhibits localized magnon edge states, and the existence of localized edge states is unique to a certain periodicity direction relative to the crystallographic direction in the stacking order with broken rotational symmetry.

DOI: 10.1103/kd5v-grhn

I. INTRODUCTION

Magnonics, a study of collective magnetization excitation in magnetic materials, emerged as a promising platform to realize less-dissipative and high-speed information processing [1] up to terahertz (THz) regimes. With the discovery of two-dimensional (2D) magnetic van der Waals materials at finite temperature, e.g., CrI_3 [2–4], magnonics expands to the group of 2D materials, which allows high-density magnonic devices to be realized. Furthermore, the weak van der Waals interactions between the layers and 2D nature of the magnetic van der Waals materials enable the tuning of magnetic properties via strain [5–10] and stacking [11–15]. Controls over stacking order in one multilayer system have been demonstrated by performing mechanical interlayer sliding [16], terahertz light pulse-induced interlayer shear strain [17], and ion intercalation [18]. In particular, it was shown that the terahertz light pulse induces a small interlayer sliding in WTe_2, which drives the system into a metastable electronic topological phase [17].

Terahertz magnon excitation has been directly observed in the monolayer CrI_3 via magneto-Raman spectroscopy [19], where the magnon frequency in the optic mode (4.11 THz) is mainly attributed to the first-nearest-neighbor spin-exchange interactions, while that in the acoustic mode (0.07 THz) is linked to the magnetic anisotropy. In both spin-exchange interactions and the magnetic anisotropy, the I atom has two roles, in which the I atom mediates the isotropic spin-exchange interactions between Cr atoms, and the strong spin-orbit coupling (SOC) in I atom induces the anisotropic spin-exchange interactions, the so-called Kitaev interactions, resulting in large magnetic anisotropy energy up to 1 meV per unit cell [20–22]. Additionally, several experimental and theoretical works hinted that the Dzyaloshinskii-Moriya interactions (DMIs) drive topological magnon in the CrI_3, in addition to the first-nearest-neighbor Kitaev interactions [23–27].

Attempts to tune magnetic interactions and magnonic properties of the CrI_3 have been demonstrated by placing the CrI_3 onto nonmagnetic metal substrate and depositing nonmagnetic semimetal atoms on the CrI_3. In CrI_3/Au(111), the magnetic anisotropy energy is stacking order dependent and can be enhanced up to 50% [28]. However, a large lattice mismatch between CrI_3 and bulk Au(111) substrate requires a large chemical unit cell of CrI_3, which can lead to magnon mode splitting and enhanced magnon-magnon scattering. In the bilayer system with nonmagnetic semimetallic atom, e.g., As, Sb, or Bi, deposited on monolayer CrI_3, the magnetization of the CrI_3 was used as a knob to control the nonmagnetic semimetals electronic band gap and the electronic topological phase [29]. While the magnetic anisotropy energy and Curie temperature in the CrI_3 are enhanced in the presence of the nonmagnetic semimetallic elements, the effect of the elements on the THz magnon excitation in the CrI_3 remains unaddressed. Additionally, depositing thin layer of semimetal atoms on the CrI_3 allows keeping similar lattice constant and chemical unit cell of pristine CrI_3, and the stacking orders can be controlled after the deposition on the CrI_3 [16,29].

In this work, we demonstrated the modulation of magnetic and topological magnonic properties in multiple stacking orders of bilayers CrI_3/As using first-principles calculations and linear spin-wave theory. By considering six possible stacking orders of CrI_3/As, we determined three energetically stable stacking orders, which are symmetrically distinct, and we observed modulation of magnetism and magnonic properties in them. First, the isotropic spin-exchange constants are enhanced up to 100% due to the splitting of Cr

*Contact author: 423db01@m.mie-u.ac.jp

 ©2026 American Physical Society

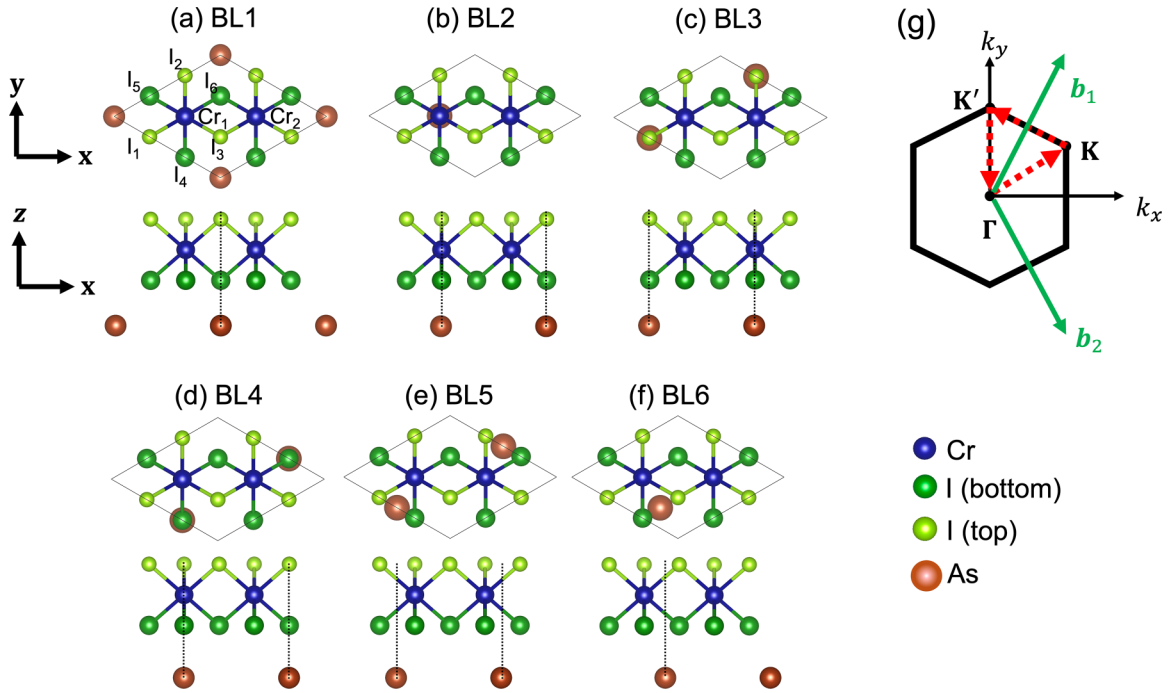

FIG. 1. Six symmetrically distinct stacking order of CrI_3/As bilayers, labeled as (a) BL1, (b) BL2, (c) BL3, (d) BL4, (e) BL5, and (f) BL6, where the As atom position is varied relative to the $\sqrt{3} \times \sqrt{3}$ unit cell of CrI_3. In (a)–(f), top and side view of each stacking order are presented. The blue, dark green, light green, and brown spheres denote Cr, I at the upper CrI_3 sublayer, I at the bottom CrI_3 sublayer, and As atoms, respectively. (g) Brillouin zone of the CrI_3 with high-symmetry point $\mathbf{\Gamma}$, $\mathbf{K}$, and $\mathbf{K}'$, and the $\mathbf{k}$ path for magnon dispersion and Berry curvature plotting is shown by red dashed lines. The reciprocal lattice vectors, $\mathbf{b}_1$ and $\mathbf{b}_2$, are also shown in solid green lines. In (a), the index for I atoms $i \in \{1, \cdots, 6\}$ and that of Cr atoms $j \in \{1, 2\}$ are also indicated.

d orbitals near the Fermi level induced by the As atom. Second, the addition of As monolayer breaks the inversion symmetry between the first-nearest-neighboring Cr atoms via interfacial charge transfer, which gives rise to finite DMIs of first-nearest-neighboring Cr atoms and enhances those of second-nearest-neighboring Cr atoms. Third, localized magnon edge states in a one-dimensional (1D) nanoribbon geometry show that three stacking orders of CrI_3/As bilayer exhibit different topological magnonic properties depending on the broken symmetries present in the system. The results in the effect of the As can also be extended to the case of bilayer CrI_3/Sb or CrI_3/Bi.

This paper is organized as follows. In Sec. II, we introduce the multiple stacking orders of CrI_3/As bilayers, and present methods of first-principles calculation of spin-exchange constants based on magnetic force theorem, and magnon dispersion calculation based on linear spin-wave theory. In Sec. III, we present the results and discussion for spin-exchange interactions, DMIs, and topological magnons of CrI_3 under the addition of the As triangular lattice. Magnon dispersions for one-dimensional nanoribbon geometry in each stacking order are also presented to emphasize the distinct topological magnon properties. We summarize our work in Sec. IV.

II. METHODS

A. Multiple CrI_3/As stacking orders

We initially considered six symmetrically distinct stacking orders of CrI_3/As, as shown in Figs. 1(a)–1(f), where $\sqrt{3} \times \sqrt{3}$ CrI_3 unit cell was used, and the triangular lattice As was variably positioned relative to the CrI_3, labeled as BL1–BL6. In the monolayer (ML) CrI_3 with 2D space group $P31m$, trigonal distortion reduces a perfect octahedron O_h point group symmetry of Cr atoms into D_{3d}. Under the addition of the As monolayer, the 2D space group symmetry of BL1 remains preserved to that of ML, while the point group of two Cr atoms in the unit cell is further reduced to C_{3v}. The threefold rotational symmetry around the Cr atoms is broken in the BL3–BL6. The vertical mirror symmetry in the BL2 and BL6 is broken, which results in two Cr atoms in the unit cell having symmetrically inequivalent surroundings. The details of the 2D space group and point group of two Cr atoms in the unit cell are shown in Appendix A. These symmetrically distinct stacking orders enable us to observe how isotropic and anisotropic spin-exchange interactions and hence magnon propagation are modulated under the symmetry breaking induced by the triangular lattice As monolayer.

B. Calculation details

We performed electronic structure calculations based on density functional theory (DFT) in full-potential linearized augmented plane wave (FLAPW) framework [30]. Generalized gradient approximation with Hubbard U (GGA+U) and DFT-D2 correction were employed to treat strongly correlated electrons in Cr d orbitals ($U_{\text{eff}} = 3.0$ eV) [31,32] and van der Waals interactions between layers, respectively. Muffin tin sphere radii of 1.16, 1.27, and 1.30 Å were employed for Cr, I, and As atoms, respectively. Plane wave cutoff $|\mathbf{k} + \mathbf{G}| \leqslant$

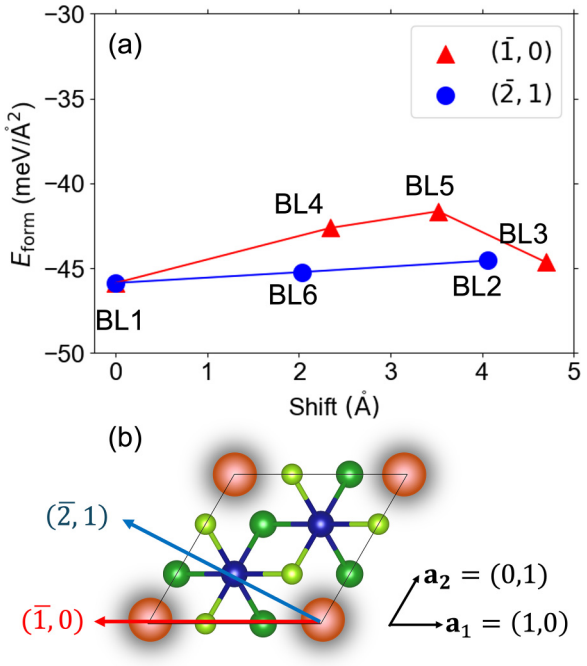

FIG. 2. (a) Formation energy per unit cell area, E_{form}, of six stacking orders bilayers BL1-BL6 in the unit of meV/Å^2 as a function of the As monolayer shift relative to the fixed CrI_3 in the BL1. The two shift vectors, along $(\bar{2}, 1)$ and $(\bar{1}, 0)$, are shown in (b). The stacking orders that are related to the BL1 via As atom shift along $(\bar{2}, 1)$ direction are denoted by the blue circles and line, while those are related to the BL1 via As atom shift along $(\bar{1}, 0)$ are denoted by the red triangles and line, where the $\mathbf{a}_1$ and $\mathbf{a}_2$ are the primitive lattice vectors [59].

7.37 Å^{-1} was used for plane wave expansion in reciprocal space. Lattice constant of 7.04 Å was obtained from geometry optimization of a freestanding monolayer (ML) CrI_3 via Murnaghan equation. The interlayer distance between CrI_3 and As was force optimized with a convergence criterion for atomic force, 0.005 htr/Å in each stacking order. The $15 \times 15 \times 1$ **k**-point mesh was used for Brillouin zone (BZ) sampling that ensures the convergence of the spin-exchange constants.

Formation energies per unit cell area, E_{form}, of each CrI_3/As stacking were calculated by the following equation,

$$E_{\text{form}} = \left(E_{CrI_3/As} - E_{CrI_3} - E_{As}\right)/A, \tag{1}$$

where A is the area of the unit cell, $E_{CrI_3/As}$ is the total energy of a CrI_3/As stacking order, and E_{CrI_3} and E_{As} are the total energy of a freestanding ML CrI_3 and As, respectively. The BL1 has the lowest E_{form} among them, with $E_{\text{Form}} = -45.87$ meV/Å^2, and the E_{form} of five other stacking orders are plotted in Fig. 2. The magnitudes of E_{form} of the six CrI_3/As bilayers range from 40 to 45 meV/Å^2, which are stronger than typical van der Waals interactions [33] but weaker than the covalent bond [34]. The interaction between the CrI_3 and As layers is classified as a weak interfacial charge transfer in the BL1 and BL2 stacking orders while as a weak covalent bond in the BL6 stacking order, as shown in the Supplemental Material in detail [35]. For comparison, the exfoliation energies in monolayer graphenes and phosphorenes are 32 and 23 meV/Å^2 [36]. Then, the stacking orders are grouped based on the direction of the As monolayer shift relative to the fixed CrI_3 in the BL1 stacking order, as shown in Fig. 2(a). The BL2 and BL6 are obtained from the BL1 by performing a shift of the As monolayer relative to a fixed CrI_3 along $(\bar{2}, 1)$ direction, where the notation of the shift direction is written in primitive lattice vectors $(\mathbf{a}_1, \mathbf{a}_2)$, as seen in Fig. 2(b). On the other hand, a shift of the As monolayer along $(\bar{1}, 0)$ gives the BL3, BL4, and BL5. In this work, only the BL1, BL2, and BL6 are discussed, as they correspond to the three stacking orders with the lowest E_{form}. Additionally, the BL1, BL2, and BL6 enable us to simulate the effect of 2D space group ($P31m$, $P3$, and $P1$) and point group symmetry (C_{3v}, C_{3v}, and C_1) changes on the magnetic interactions and topological magnons.

The spin-exchange constants were obtained via magnetic force theorem and the linear response approach [37–39]. The spin-exchange constant between Cr atom at site τ in the unit cell at the origin and that at site τ' in the unit cell $R_{l'}$ is given as

$$J^{\alpha\beta}_{\tau,\mathbf{R}_{l'}+\tau'} = \sum_{\mathbf{k},\mathbf{q},n,n'} \frac{f_{\mathbf{k},n} - f_{\mathbf{k}+\mathbf{q},n'}}{\varepsilon_{\mathbf{k},n} - \varepsilon_{\mathbf{k}+\mathbf{q},n'}} \langle \Psi_{\mathbf{k},n} | [\boldsymbol{\sigma} \times \mathbf{B}_{\tau}]_{\alpha} | \Psi_{\mathbf{k}+\mathbf{q},n'} \rangle \times \langle \Psi_{\mathbf{k}+\mathbf{q},n'} | [\boldsymbol{\sigma} \times \mathbf{B}_{\tau'}]_{\beta} | \Psi_{\mathbf{k},n} \rangle e^{-i\mathbf{q}\cdot\mathbf{R}_{l'}}, \tag{2}$$

where $\boldsymbol{\sigma}$ and $\mathbf{B}_{\tau}$ are Pauli matrices and the effective local magnetic field at site τ, respectively. The $\varepsilon_{\mathbf{k},n}$ and $\Psi_{\mathbf{k},n}$ are one-electron energies and wave functions, respectively, for band n at point $\mathbf{k}$ in the BZ obtained by solving Kohn-Sham equations. The α and β run over the global cartesian coordinates $\{x, y, z\}$. The anisotropic spin-exchange constants, which consist of nine constants from J^{xx} to J^{zz} for each bond, were obtained under spin-orbit correction to the $\varepsilon_{\mathbf{k},n}$ and $\Psi_{\mathbf{k},n}$, and the isotropic spin-exchange constants, denoted as J^{ex}_{ij}, were obtained by taking the eigenvalues average of the diagonalized symmetric spin-exchange matrix for each bond. Implementation of the spin-exchange constants calculation based on the magnetic force theorem in the FLAPW framework is given in Supplemental Material in detail [35].

The magnon dispersions were obtained by solving the spin Hamiltonian model via linear spin-wave theory [40]. The spin Hamiltonian is written as,

$$\hat{H} = \frac{1}{2} \sum_{\alpha,\beta}^{\{x,y,z\}} \sum_{l,l',\tau,\tau'} J^{\alpha\beta}_{\mathbf{R}_l+\tau,\mathbf{R}_{l'}+\tau'} S^{\alpha}_{\tau} S^{\beta}_{\tau'} \tag{3}$$

where S^{α}_{τ} is the component of spin operator at site τ in cubic direction, $\alpha \in \{x, y, z\}$. By performing Holstein-Primakoff [41], Fourier, and Bogoliubov transformation [42,43], magnon dispersions in reciprocal space were obtained, and ferromagnetic resonance frequencies were taken as magnon frequencies at $\boldsymbol{\Gamma}$.

III. RESULTS AND DISCUSSIONS

A. Isotropic spin-exchange constants

For the freestanding ML CrI_3, the isotropic spin-exchange constant is mainly dominated by the first-nearest-neighbor and followed by second-nearest-neighbor interactions, denoted as $J^{\text{ex}}_{(1)}$ and $J^{\text{ex}}_{(2)}$, respectively. Our results show a good agreement with previous first-principles calculations results

TABLE I. First- and second-nearest-neighbors spin-exchange constants, $J^{ex}_{(1)}$ and $J^{ex}_{(2)}$, and magnetic anisotropy energy from anisotropic spin-exchange interactions, ΔE, of a freestanding monolayer CrI_3 in meV obtained in the present work, density functional theory (DFT) calculations based on projector augmented wave (PAW) under local density approximation (LDA) [20], and generalized gradient approximation (GGA) [49] with different Hubbard correction U and experiment of Raman spectroscopy [50].

	$J^{ex}_{(1)}$	$J^{ex}_{(2)}$	ΔE
Present work	–2.32	–0.46	1.35
Theory [PAW+LDA+four-state method (U = 0.5 eV)] [20]	–2.46		1.11
Theory [PAW+GGA+four-state method (U = 4 eV)] [49]	–2.56	–0.64	
Experiment (Raman spectroscopy) [50]	–2.73		

under four-states method [48], isotropic total energy mapping [49], and Raman spectroscopy measurement [50], as shown in Table I. The $J^{ex}_{(1)}$ and $J^{ex}_{(2)}$ have a negative sign, which implies ferromagnetic (FM) coupling between magnetic moments of Cr atoms is preferable, confirming the ferromagnetism in ML CrI_3 [3,50]. The dominant FM coupling between Cr atoms ($J^{ex}_{(1)}$) satisfies the Goodenough-Kanamori rules [51,52], in which the nearly 90° superexchange cation-anion-cation (Cr-I-Cr) stabilizes the ferromagnetic alignment between two nearest Cr atoms.

In the ML CrI_3, the partial density of states (PDOS), projected along the Cr-I bond direction, is shown in Fig. 3(a), and the corresponding energy levels are shown in Figs. 3(b) and 3(c) in undistorted and trigonal-distorted structures, respectively. One Cr atom, coordinated with six I atoms, forms edge-sharing octahedra, which results in the octahedral crystalline electric field (CEF), splitting Cr d orbitals into occupied threefold t_{2g} state and unoccupied twofold e_g state for the majority spin electrons. Ferromagnetic coupling between first-nearest-neighbor Cr atoms, indicated by negative $J^{ex}_{(1)}$, can be explained by Hubbard model [53]. The empty I p states and Cr e_g states above the Fermi level allow electrons from the occupied t_{2g} states of one Cr atom to be excited into the empty e_g states of another Cr atom via I p states, by keeping the electron spin. The unchanged electron spin during hopping processes results in the favored ferromagnetic coupling between the first-nearest-neighboring Cr atoms. In real space, one of the electron hopping channel mediated by I atom is from Cr $d_{x'^2-y'^2}$ $\overset{pd\sigma}{\longleftrightarrow}$ I $p_{x'}$ $\overset{pd\pi}{\longleftrightarrow}$ Cr $d_{x'y'}$, where the primes indicate the rotated coordinate axes along the octahedron axes, as shown in Fig. 3.

In the presence of the As monolayer, the first-nearest-neighbor spin-exchange constant undergoes an enhancement depending on the As atom position relative to CrI_3 layer, as shown in Fig. 4(a). We split the first-nearest-neighbor spin-exchange constants into three contributions from each bond, labeled as $J^{ex}_{(1),a}$, $J^{ex}_{(1),b}$, and $J^{ex}_{(1),c}$, as shown in the Figs. 4(b)–4(d) for stacking order BL1, BL2, and BL6, respectively. The rotational symmetry of the bilayers, induced by the As monolayer, reflects in the symmetry between $J^{ex}_{(1),a}$, $J^{ex}_{(1),b}$, and $J^{ex}_{(1),c}$, as shown in Figs. 4(b)–4(d). In the BL1 and BL2, the rotational symmetry around the Cr atom remains similar to that in the ML CrI_3, as can be seen in Figs. 4(b) and 4(c), resulting in small uniform enhancements of $J^{ex}_{(1)}$ in all bonds.

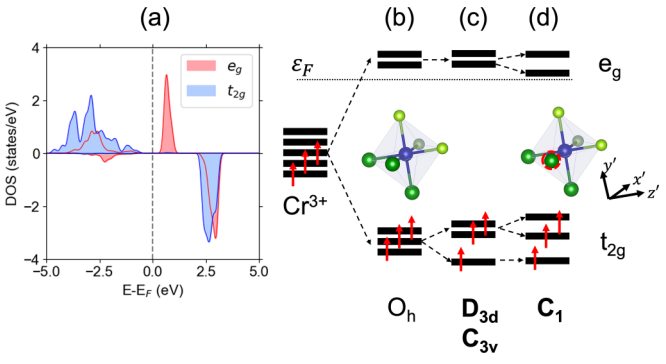

FIG. 3. (a) Partial density of states (PDOS) of Cr d states of a freestanding monolayer CrI_3 without SOC, where the quantum axes are projected into the orthogonal axes along to Cr-I of an octahedron, denoted as $\{x', y', z'\}$. Red and blue shaded areas represent e_g and t_{2g} states, respectively. The orbital splitting of d states in the CrI_3, under (b) O_h, (c) D_{3d} and C_{3v} point group, and (d) distortion of the octahedron into C_1 point group [59].

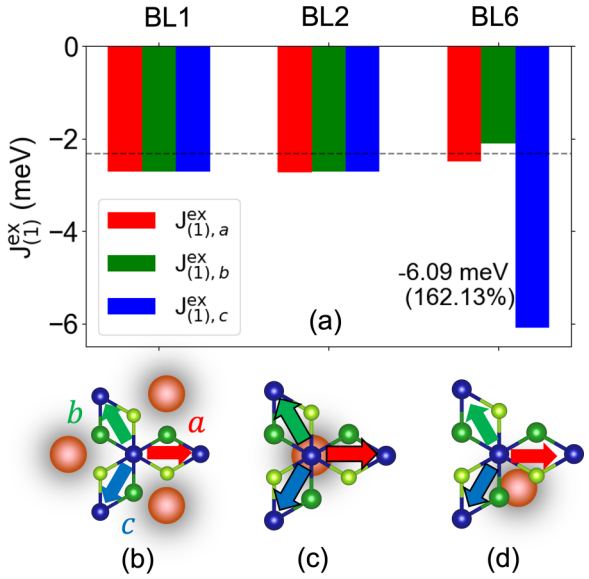

FIG. 4. (a) First-nearest-neighbor spin-exchange constants decomposed into three first-nearest-neighbor bonds, a, b, and c in meV, colored in red, green, and blue, respectively. The horizontal dashed line in (a) represents the $J^{ex}_{(1)}$ of monolayer CrI_3. Three first-nearest-neighboring Cr-Cr bonds for stacking order (b) BL1, (c) BL2, and (d) BL6, where blue, dark green, light green, and brown spheres represent Cr, I from bottom CrI_3 sublayer, I from upper CrI_3 sublayer, and As atoms. The red, green, and blue arrows in (b)–(d) represent a, b, and c bonds [59].

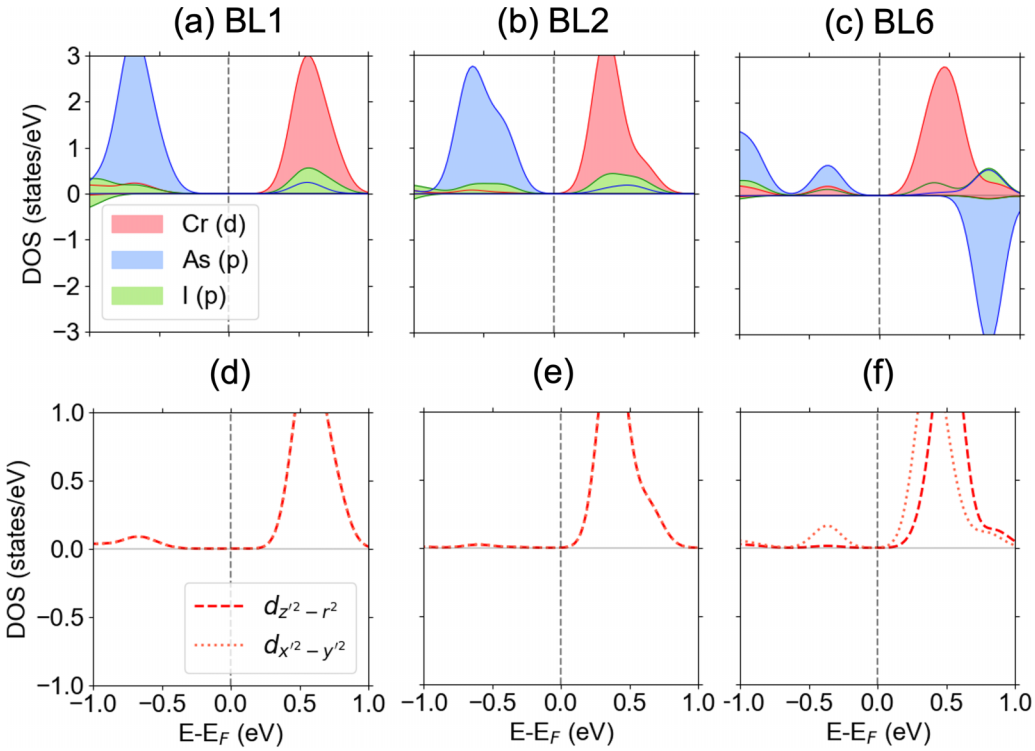

FIG. 5. Partial density of states (PDOS) of Cr d states, I p states, and As p states in three CrI_3/As stacking orders, (a) BL1, (b) BL2, and (c) BL6. In (a)–(c) figures, red, green, and blue shaded areas represent Cr d, I p, and As p states, respectively. PDOS of Cr t_{2g} and e_g states, projected along a Cr-I bond that has As atom nearby, for stacking order (d) BL1, (e) BL2, and (f) BL6. In (d)–(f), red dashed and dotted lines represent Cr $d_{z'^2-r^2}$ and $d_{x'^2-y'^2}$, respectively, while the PDOS of t_{2g} states are negligible in this energy range [59]. The PDOS of Cr d orbitals in the CrI_3/As bilayers under spin-orbit coupling correction are presented in the Supplemental Material [35].

On the other hand, in the BL6, one of the three $J^{ex}_{(1)}$'s is enhanced by more than 100% from that of ML CrI_3, while the other two bonds are relatively unchanged. In the BL6 stacking order, the bond that undergoes enhancement of $J^{ex}_{(1)}$ contains an As atom close to an I atom from the bottom CrI_3 sublayer.

In the CrI_3/As bilayers, the PDOS of Cr d, I p, and As p states are shown in Figs. 5(a)–5(c) for the BL1, BL2, and BL6, respectively. For the BL1 and BL2, the peak around 0.5 eV below Fermi level only consists of I p and As p states, without Cr d states. However, we observed a small peak around 0.5 eV below the Fermi level in the BL6, consisting of Cr d, I p, and As p states. By projecting the Cr d states along the Cr-I bond that has the As atom nearby, the PDOS of Cr t_{2g} and e_g are shown in Figs. 5(d)–5(f) for the BL1, BL2, and BL6, respectively. In the BL1 and BL2, the O_h point group is distorted into C_{3v}, which only results in the splitting of t_{2g} states and leaves the e_g states degenerate, as shown in Fig. 3(c). Since the t_{2g} states are fully occupied and far below the Fermi level, the $J^{ex}_{(1)}$ in BL1 and BL2 does not change significantly compared to that in BL6. However, in the BL6, the small peak around 0.5 eV below the Fermi level arises from the degeneracy lifting between $d_{z'^2-r^2}$ and $d_{x'^2-y'^2}$ states, which are unoccupied above the Fermi level in the freestanding ML CrI_3. The degeneracy lifting in the e_g states is mainly attributed to the distorted octahedral CEF in the presence of As monolayer close to the one of the six edge-sharing I atoms, reducing the symmetry in the D_{3d} point group symmetry around the Cr atom into C_1, as shown in Fig. 3(d) and Table III in Appendix A. The small peak around 0.5 eV below the Fermi level lowers the energy requirement for electrons to hop from the t_{2g} states into the e_g states, increasing the probability of electrons hopping from between Cr atoms via the distorted I atom, and consequently increasing the spin-exchange constant. Additionally, for all stacking orders, the interaction between As p and I p orbitals reduces the energy gap, which also allows more electron hopping between first-nearest-neighboring Cr atoms via the I atom and enhances the spin-exchange constants.

B. Anisotropic spin-exchange interactions: Dzyaloshinskii-Moriya interactions (DMIs)

The spin-exchange constants where $\alpha \neq \beta$ in Eq. (2) contain the antisymmetric DMIs, which are the key magnetic interactions that drive topological magnons in magnetic materials. The DMI vectors are related to the off-diagonal

TABLE II. The average charge density difference between two I atoms in each first- and second-nearest-neighbor bond, $\Delta\bar{n}_{(1)}$ and $\Delta\bar{n}_{(2)}$, and the change of As atom charge density under stacking with the CrI_3, δn_{As}, in the unit of e bohr^{-3}.

	ML	BL1	BL2	BL6
$\Delta\bar{n}_{(1)}$ ($\times 10^{-3}$)	0.00	1.21	1.29	9.36
$\Delta\bar{n}_{(2)}$ ($\times 10^{-3}$)	0.00	1.21	1.29	13.21
δn_{As} ($\times 10^{-2}$)		–1.47	–0.79	–1.01

TABLE III. The 2D space group and point group of Cr atoms in the unit cell of monolayer (ML) CrI_3 and six stacking order of CrI_3/As bilayer. Under the trigonal lattice distortion and addition of the As monolayer, the O_h point group reduces into some lower point group symmetries.

Stacking order	2D Space group	Point group
ML	$P31m$	D_{3d}
BL1	$P31m$	C_{3v}
BL2	$P3$	C_{3v}
BL3	$P1m$	C_{3v}
BL4	$P1m$	C_1
BL5	$P1m$	C_1
BL6	$P1$	C_1

spin-exchange tensors, which are given by,

$$D_{ij}^{z} = \tfrac{1}{2}\left(J_{ij}^{xy} - J_{ij}^{yx}\right), \quad D_{ij}^{y} = \tfrac{1}{2}\left(J_{ij}^{zx} - J_{ij}^{xz}\right),$$
$$D_{ij}^{x} = \tfrac{1}{2}\left(J_{ij}^{yz} - J_{ij}^{zy}\right). \tag{4}$$

Based on the magnetic easy axis directions, i.e., along out-of-plane direction for ML, BL1, and BL2, while in-plane y direction for BL6, as mentioned in Appendix B, the components of DMI vectors are grouped into the DMI parallel to the magnetic easy axis, $D_{ij}^{\parallel}$, and DMI perpendicular to the magnetic easy axis, $D_{ij}^{\perp}$, as given by,

$$D_{ij}^{\parallel} = \begin{cases} \left|D_{ij}^{z}\right| & \text{for ML, BL1, and BL2,} \\ \left|D_{ij}^{y}\right| & \text{for BL6,} \end{cases}$$
$$D_{ij}^{\perp} = \begin{cases} \sqrt{\left(D_{ij}^{x}\right)^2 + \left(D_{ij}^{y}\right)^2} & \text{for ML, BL1, and BL2,} \\ \sqrt{\left(D_{ij}^{x}\right)^2 + \left(D_{ij}^{z}\right)^2} & \text{for BL6.} \end{cases} \tag{5}$$

The $D_{ij}^{\parallel}$ couples the transversal components of oscillating magnetization, e.g., x with y component of magnetization for magnetic easy axis along z direction. On the other hand, the $D_{ij}^{\perp}$ couples the transversal component of oscillating magnetization with the quantized component of oscillating magnetization, e.g., x/y with z component of magnetization for magnetic easy axis along z direction. If the $D_{ij}^{\perp}$ is larger than the isotropic spin-exchange constants, $D_{ij}^{\perp}$ induces a noncollinear spin-canting structure, while weak $D_{ij}^{\perp}$ induces magnon damping via three-magnon interactions [54].

The DMIs in the ML CrI_3 are shown in Figs. 6(a) and 6(e), where the first-nearest-neighbor DMIs, $D_{(1)}^{\parallel}$ and $D_{(1)}^{\perp}$, are zero, while the second-nearest-neighbor DMIs, $D_{(2)}^{\parallel}$ and $D_{(2)}^{\perp}$, are nonzero. The magnitude of $D_{(2)}^{\parallel}$ is around 0.04 meV [Fig. 6(a)], which is smaller than that of $D_{(2)}^{\perp}$ around 0.1 meV [Fig. 6(e)]. The existence of I atoms already fulfills the requirement of the SOC for the finite DMI, but the requirement of having broken inversion symmetry at the center of the bond depends on the geometry of the bond. The first-nearest-neighboring Cr atoms form two 90° superexchange paths via two I atoms, and the inversion symmetry at the center of Cr-Cr bond is preserved, as shown in Figs. 7(a) and 7(b) for the side and top view. This geometry of the first-nearest-neighboring Cr atoms results in zero first-nearest-neighbor DMIs, according to Moriya's theory [55]. On the other hand, the second-nearest-neighboring Cr atoms form a superexchange path mediated by two consecutive I atoms. Under trigonal distortion, the displacements of two I atoms break the inversion symmetry at the center of Cr-Cr atoms, and finite DMI appears. According to Moriya's theory [55], the DMI vector points along the perpendicular direction relative to the twofold rotation axis indicated by the red arrow in Fig. 7(d). This results in $\mathbf{D}_{(2)}$ pointing along z direction and

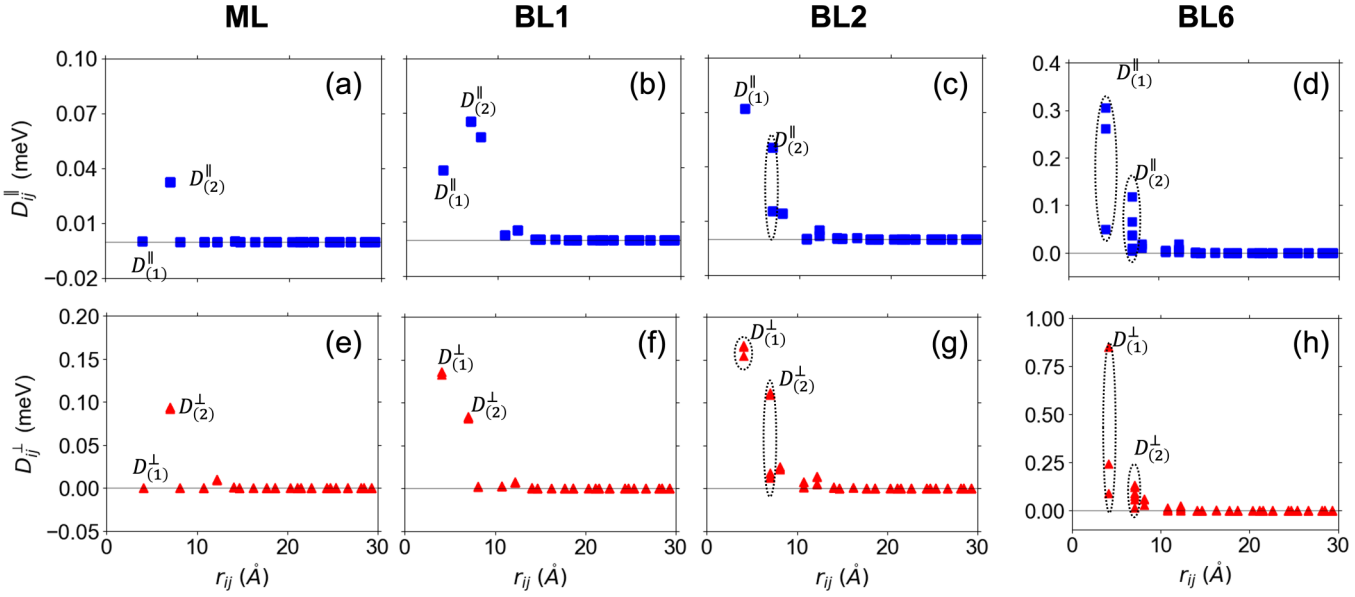

FIG. 6. The Dzyaloshinskii-Moriya interactions (DMIs) component parallel to the magnetic easy axis, $D_{ij}^{\parallel}$, in unit of meV as a function of interactions distance, r_{ij}, in unit of Å for the (a) monolayer (ML) CrI_3, (b) BL1, (c) BL2, and (d) BL6 CrI_3/As bilayers. The DMIs component perpendicular to the magnetic easy axis, $D_{ij}^{\perp}$, for the (e) ML, (f) BL1, (g) BL2, and (h) BL6 CrI_3/As bilayers. In all figures, the first- and second-nearest-neighbor DMI are denoted by subscripts (1) and (2), respectively [59].

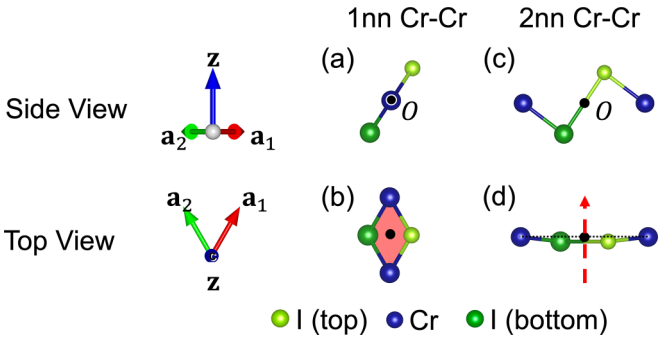

FIG. 7. The first-nearest-neighboring (1nn) Cr atoms from two superexchange paths mediated by two I atoms, as viewed from (a) side and (b) top. The second-nearest-neighboring (2nn) Cr atoms mediated by two consecutive I atoms, as viewed from (c) side and (d) top. In (a)-(d), blue, dark green, and light green denote Cr, I at bottom, and top of CrI_3 sublayer, respectively. The black circle O represents the inversion point in each bond. Red plane in (b) represents a plane that contains the first-nearest-neighboring Cr atoms with the two mediating I atoms. Red vector in (d) represents the twofold rotation axis that leaves the Cr-I-I-Cr unchanged.

Cr-Cr bond, which confirms the finite values of $D^{\parallel}_{(2)}$ and $D^{\perp}_{(2)}$, respectively.

In the CrI_3/As bilayers, the first-nearest-neighbor DMIs increase to larger than 0.1 meV, while the second-nearest-neighbor DMIs increase slightly around 0.1 meV. The increase of the first-nearest-neighbor DMIs are mainly attributed to the increase of $D^{\perp}_{(1)}$ to greater than 0.13 meV for BL1 and BL2 while greater than 0.5 meV for BL6, as shown in Figs. 6(f)–6(h). On the other hand, $D^{\parallel}_{(1)}$ increases to less than 0.1 meV for BL1 and BL2 and less than 0.2 meV for BL6, as shown in Figs. 6(b)–6(d). For the second-nearest-neighbor DMIs, we also observed the increase of the $D^{\parallel}_{(2)}$ in the bilayer system, as shown in Figs. 6(b)–6(d). Particularly, the maximum increases of $D^{\parallel}_{(2)}$ in the bilayer are more than twice from 0.04 meV in ML to 0.07 meV in BL1, 0.05 meV in BL2, and up to 0.1 meV in BL6, while the largest value of $D^{\perp}_{(2)}$ in the bilayers is relatively similar to that in the ML.

The magnetic ground states of each CrI_3/As stacking order are assumed to be collinear ferromagnetic, based on the comparison between the $D^{\perp}_{(1)}/J^{\rm ex}_{(1)}$ and $D^{\perp}_{(2)}/J^{\rm ex}_{(1)}$ in the present work and those in previous magnetic ground-state calculations. Previous Monte Carlo simulations on the honeycomb Janus monolayer CrI_3 showed that $D^{\perp}_{(1)}/J^{\rm ex}_{(1)}$ larger than 0.15 results in noncollinear spin textures as magnetic ground state [44], and Luttinger-Tisza calculations demonstrated that $D^{\perp}_{(2)}/J^{\rm ex}_{(1)}$ less than 0.69 results in collinear ferromagnetic as the magnetic ground state [45–47]. In the BL1, BL2, and BL6, we found that $D^{\perp}_{(1)}/J^{\rm ex}_{(1)}$ are all less than 0.15, and $D^{\perp}_{(2)}/J^{\rm ex}_{(1)}$ are all less than 0.05, which justifies our assumption that the magnetic ground state remains collinear ferromagnetic. The details of the $D^{\perp}_{(1)}/J^{\rm ex}_{(1)}$ and $D^{\perp}_{(2)}/J^{\rm ex}_{(1)}$ of BL1, BL2, and BL6 are given in the Supplemental Material [35].

In the BL1, BL2, and BL6, the inversion symmetry at the center of Cr-Cr bond is broken, and finite DMI in the first-nearest-neighboring Cr atoms appears and points along the normal vector of the red plane in Fig. 7(b) according to Moriya's theory [55], which results in finite $D^{\parallel}_{(1)}$ and $D^{\perp}_{(1)}$ due to the red plane being tilted relative to the global coordinate axes. To understand the origin of the increase of the $|D_{(1)}|$, the difference between the charge density of two I atoms that mediate two first-nearest-neighboring Cr atoms is calculated, and the average between the three first-nearest-neighbor bonds is defined by,

$$\Delta\bar{n}_{(1)} = \frac{\left|n_{\rm I_3} - n_{\rm I_6}\right| + \left|n_{\rm I_2} - n_{\rm I_5}\right| + \left|n_{\rm I_1} - n_{\rm I_4}\right|}{3}, \qquad (6)$$

where the $\rm I_i$ with $i = 1, ..., 6$ are shown in Fig. 1(a). The averages charge density difference between two I atoms in each first-nearest-neighbor bond, $\Delta\bar{n}_{(1)}$, are summarized in the Table II. From BL1 to BL6, the $\Delta\bar{n}_{(1)}$ increases, which correspond to the increasing trend of $|D_{(1)}|$ between BL1, BL2, and BL6. The finite $\Delta\bar{n}_{(1)}$ is attributed to the interfacial charge transfer from the electrons in the As monolayer to the CrI_3 layer, and the transferred charges are redistributed across the layer. This mechanism is indicated by the decreasing charge density of As atoms $\delta n_{\rm As}$, as shown in the Table II, which is defined as the charge density of the As atom in the bilayer CrI_3/As subtracted by that in the freestanding ML As, $n_{\rm As,BLx}$ - $n_{\rm As,ML}$. The increases of $|D^{(2)}|$ are also traced by calculating the difference between charge density of two consecutive I atoms that mediate second-nearest-neighboring Cr atoms and taking the average between all second-nearest-neighbor bonds, as defined by

$$\Delta\bar{n}_{(2)} = \frac{\left|n_{\rm I_2} - n_{\rm I_4}\right| + \left|n_{\rm I_1} - n_{\rm I_6}\right| + \left|n_{\rm I_3} - n_{\rm I_5}\right| + \left|n_{\rm I_3} - n_{\rm I_4}\right| + \left|n_{\rm I_2} - n_{\rm I_6}\right| + \left|n_{\rm I_1} - n_{\rm I_5}\right|}{6}. \qquad (7)$$

The $\Delta\bar{n}_{(2)}$ are summarized in the Table II, and the increasing trend of $\Delta\bar{n}_{(2)}$ from BL1 to BL6 are also shown, which also due to the interfacial charge transfer from the As monolayer to the CrI_3 layer.

C. Topological magnon

1. Magnon dispersion in 2D geometry

Using the spin-exchange constants obtained via magnetic force theorem, the magnon dispersion of a ML CrI_3 is calculated in Fig. 8(a) for two magnon modes, optic (red line) and acoustic (blue line) modes for higher- and lower-frequency modes, respectively.

At $\mathbf{\Gamma}$, the acoustic mode represents magnetic moment precession where all Cr atoms are in phase, as seen in Fig. 9(a), while the optic mode represents a uniform magnetic moment precession where first-nearest-neighboring Cr atoms have a 180° phase difference, as seen in Fig. 9(b). In the optic mode, the phase difference of 180° between first-nearest-neighbor Cr atoms results in antiparallel alignment between the transversal

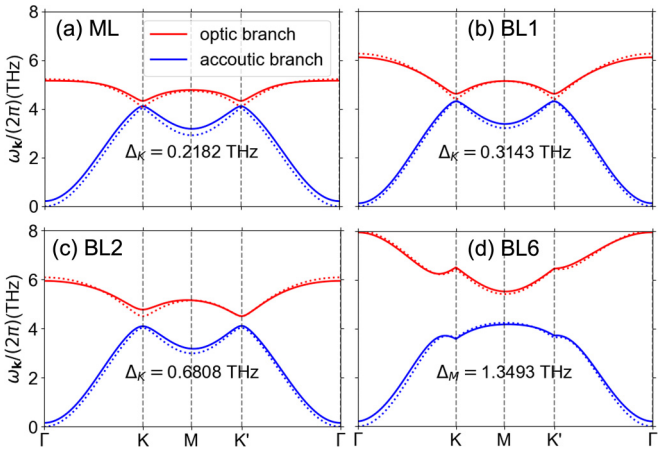

FIG. 8. Magnon dispersion, $\omega_{\mathbf{k}}$, of (a) ML CrI_3, bilayer CrI_3/As (b) BL1, (c) BL2, and (d) BL6 in THz. The dotted line represents the magnon dispersion obtained by only isotropic spin-exchange constants. The red and blue lines represent the optic and acoustic modes, respectively [59].

components of first-nearest-neighboring Cr magnetic moments and costs energy equal to the sum of the first-nearest-neighbor spin-exchange constants. In the acoustic mode, the magnon frequencies are mainly determined by the breaking SO(3) spin rotational symmetry from the anisotropic spin-exchange interactions and single-ion anisotropy, e.g., the difference between the energy of magnetic moment along the easy axis direction and that along a direction perpendicular to the easy axis. Magnon frequencies at **Γ**, which correspond to the FMR frequencies, were found to be 5.15 THz for the optic mode and 0.21 THz for the acoustic mode, which are in agreement with the results of magneto-Raman spectroscopy (4.11 and 0.08 THz) [19]. Had the magnetic anisotropy energy been assumed by a single-ion anisotropy term of Cr atom in the spin Hamiltonian, the acoustic FMR frequency is overestimated by more than 0.5 THz.

At **K**, a magnon frequency gap between optic and acoustic modes, $\Delta_{\mathbf{K}}$, is open under the anisotropic spin-exchange interactions, and our calculation gives 0.218 THz of $\Delta_{\mathbf{K}}$. If one considers only the isotropic spin-exchange interactions, the optic and acoustic modes at **K** and **K**′ are degenerate, as shown by dotted lines in Fig. 8(a). The magnetic moment precessions at **K** between first-nearest-neighboring Cr atoms are shown in Figs. 9(c) and 9(d), and the energies of these magnetic moment configurations in the isotropic case are given by,

$$\begin{aligned} E^{(1),\mathrm{ex}}_{\mathrm{acoustic},\mathbf{K}} &= \tfrac{1}{2}\left|J^{\mathrm{ex}}_{(1),a}\right| - \left|J^{\mathrm{ex}}_{(1),b}\right| + \tfrac{1}{2}\left|J^{\mathrm{ex}}_{(1),c}\right| = 0, \\ E^{(1),\mathrm{ex}}_{\mathrm{optic},\mathbf{K}} &= -\tfrac{1}{2}\left|J^{\mathrm{ex}}_{(1),a}\right| + \left|J^{\mathrm{ex}}_{(1),b}\right| - \tfrac{1}{2}\left|J^{\mathrm{ex}}_{(1),c}\right| = 0, \end{aligned} \tag{8}$$

and the rotational symmetry between three first-nearest-neighbor spin-exchange constants has been taken into account. This implies that the two types of magnetic moment precession are degenerate at **K** in the isotropic case, as confirmed by the magnon dispersion in the dotted lines in Fig. 8(a). Under the first-nearest-neighbor DMIs, the energies of magnetic moment configuration in Figs. 9(c) and 9(d) are given by,

$$\begin{aligned} E^{(1),\mathrm{DMI}}_{\mathrm{acoustic},\mathbf{K}} &= -D^{\parallel}_{(1)}\left(\tfrac{1}{2}\sqrt{3}\right) - D^{\parallel}_{(1)}(0) - D^{\parallel}_{(1)}\left(-\tfrac{1}{2}\sqrt{3}\right) \\ &= 0, \\ E^{(1),\mathrm{DMI}}_{\mathrm{optic},\mathbf{K}} &= -D^{\parallel}_{(1)}\left(-\tfrac{1}{2}\sqrt{3}\right) - D^{\parallel}_{(1)}(0) - D^{\parallel}_{(1)}\left(\tfrac{1}{2}\sqrt{3}\right) \\ &= 0, \end{aligned} \tag{9}$$

which implies that $D^{\parallel}_{(1)}$ does not lift the degeneracy at **K**. On the other hand, under the second-nearest-neighbor DMIs, the energies of magnetic moment configuration in Figs. 9(e) and 9(f) are given by,

$$\begin{aligned} E^{(2),\mathrm{DMI}}_{\mathrm{acoustic},\mathbf{K}} &= -D^{\parallel}_{(2)}\left(\tfrac{1}{2}\sqrt{3}\right) + D^{\parallel}_{(2)}\left(-\tfrac{1}{2}\sqrt{3}\right) \\ &\quad - D^{\parallel}_{(2)}\left(\tfrac{1}{2}\sqrt{3}\right) + D^{\parallel}_{(2)}\left(-\tfrac{1}{2}\sqrt{3}\right) \\ &\quad - D^{\parallel}_{(2)}\left(\tfrac{1}{2}\sqrt{3}\right) + D^{\parallel}_{(2)}\left(-\tfrac{1}{2}\sqrt{3}\right) \\ &= -3\sqrt{3}D^{\parallel}_{(2)}, \\ E^{(2),\mathrm{DMI}}_{\mathrm{optic},\mathbf{K}} &= -D^{\parallel}_{(2)}\left(-\tfrac{1}{2}\sqrt{3}\right) + D^{\parallel}_{(2)}\left(\tfrac{1}{2}\sqrt{3}\right) \\ &\quad - D^{\parallel}_{(2)}\left(-\tfrac{1}{2}\sqrt{3}\right) + D^{\parallel}_{(2)}\left(\tfrac{1}{2}\sqrt{3}\right) \\ &\quad - D^{\parallel}_{(2)}\left(-\tfrac{1}{2}\sqrt{3}\right) + D^{\parallel}_{(2)}\left(\tfrac{1}{2}\sqrt{3}\right) \\ &= 3\sqrt{3}D^{\parallel}_{(2)}, \end{aligned} \tag{10}$$

and this results in the frequency gap opening by $6\sqrt{3}D^{\parallel}_{(2)}$.

The presence of the As monolayer modifies the magnon dispersions, and this is shown in Figs. 8(b)–8(d) for the BL1, BL2, and BL6, respectively. The magnon frequency gap is open at **K** and **K**′ in the BL1, BL2, and BL6. To check whether the magnon frequency gap opening arises from the symmetry breaking or the anisotropic effects, we plotted the magnon dispersion with solely isotropic spin-exchange constants, as shown by the dotted lines in Figs. 8(b)–8(d) for the BL1, BL2, and BL6, respectively. In the BL1, the optic and acoustic modes at **K** and **K**′ have a larger frequency gap by almost 50% than that in ML, which is mainly due to the enhanced $D^{\parallel}_{(2)}$ by almost twice that of ML. Therefore, the frequency gap opening at **K** and **K**′ in the BL1 is mainly driven by the anisotropic origin, which is similar to what occurs in ML. In the BL2 and BL6, the magnon dispersions with solely isotropic spin-exchange interactions exhibit gap opening, which confirms the symmetry-breaking origin of the gap opening. Particularly, the degeneracy of magnon dispersion at **K** and **K**′ in the honeycomb structure is symmetrically protected by threefold rotational and vertical mirror symmetries in the lattice space, based on the spin-space symmetry analysis [56]. In the BL2 and BL6, the two Cr sublattices are no longer symmetrically related by vertical mirror operations, which results in the degeneracy lifting at **K** and **K**′. Additionally, the broken threefold rotational symmetry in lattice space of the BL6, which enters the magnon Hamiltonian via spin-exchange interactions, results in the band minimum and maximum shifting away from the **K** and **K**′, which gives rise to the unusual kink around those wave vectors [35], as seen in Fig. 8(d).

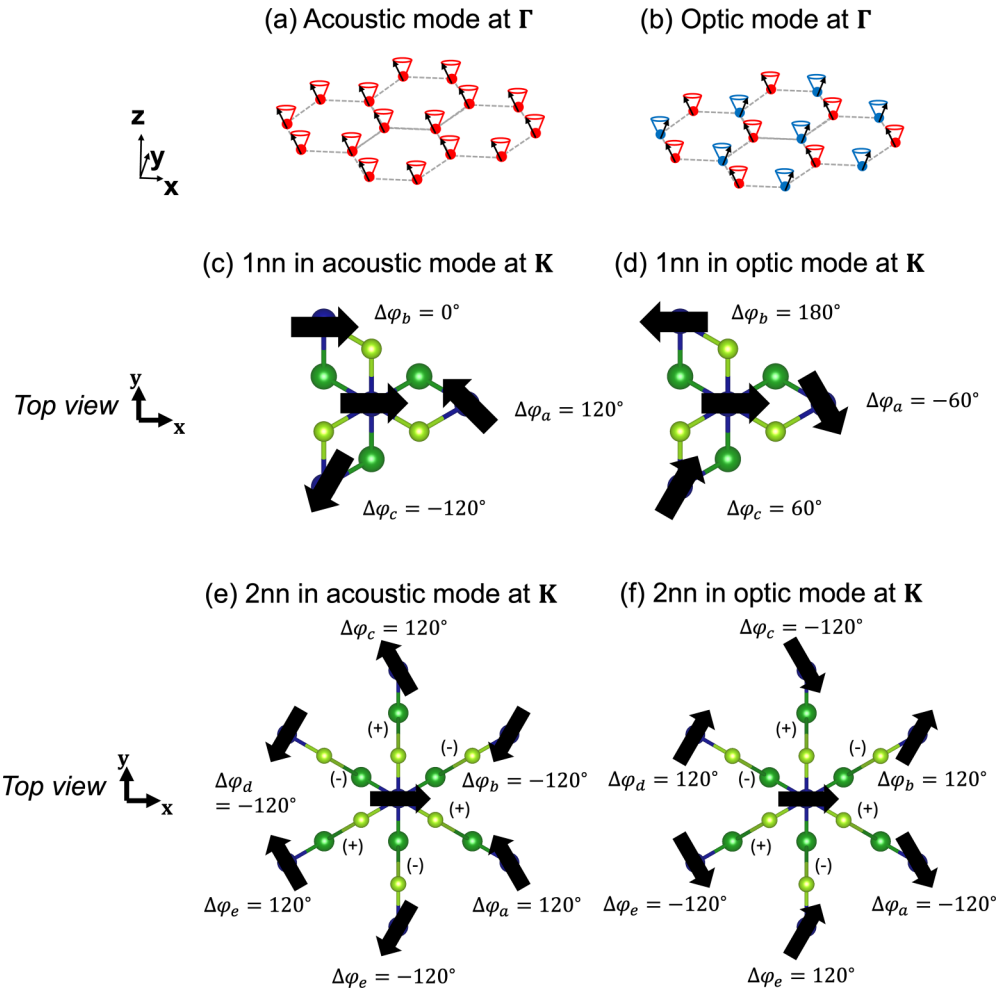

FIG. 9. Illustration of magnetic moment precession of (a) acoustic and (b) optic modes at **Γ**, where two distinct Cr sublattices have 180° phase difference and in-phase uniform precession, respectively. Top view of magnetic moment precession of (c) acoustic and (d) optic mode between first-nearest-neighbor (1nn) Cr atoms at **K**. Top view of magnetic moment precession of (e) acoustic and (f) optic mode between second-nearest-neighboring (2nn) Cr atoms at **K**. In (c)–(f), $\Delta\varphi_i$, where i is an index for the bond, represents the phase difference between each of a first-nearest-neighbor magnetic moment and the magnetic moment of the central atom. The (+) and (-) symbols in (e) and (f) represent the sign of $D^{\parallel}_{(2)}$.

2. Magnon dispersion in quasi-1D nanoribbon geometry

The topological magnon phase implies the existence of chiral localized magnon edge states that close the bulk magnon gap, and this is called bulk-boundary correspondence. To confirm the existence of magnon edge states, we investigated magnon dispersions of ML CrI_3 and bilayers CrI_3/As in a quasi-1D nanoribbon geometry with zig-zag termination, as shown in Fig. 10(a). We resolved the contribution of three Cr atoms to the magnon states, where two Cr atoms are located at the opposite edges of the nanoribbon, and one Cr is located at the middle of nanoribbon, as indicated by blue, red, and green spheres in Fig. 10(a), respectively.

In the case of ML CrI_3, the magnon dispersion is shown in Fig. 10(b), and the two localized edge states, which consist of only the Cr atom at the edges, are seen between 4.00 and 4.25 THz and cross at $\bar{\mathbf{\Gamma}}$ point. Additionally, the two localized edge states also exhibit chirality upon mirroring to both $\bar{\mathbf{\Gamma}}$ and $\bar{\mathbf{M}}$, which implies that magnons at the two edges propagate in opposite directions and confirms the topologically nontrivial phase of ML CrI_3. In the BL1 stacking order, the magnon dispersion is shown in Fig. 10(c), which has similar properties to those of the ML CrI_3 due to the similar space group symmetry, while the frequency range of localized chiral edge states is from 4.00 to 4.75 THz.

In the BL2 stacking order, magnon dispersion is shown in Fig. 10(d), and the two localized edge states have frequency ranges from 4.00 to 4.75 THz, which is wider than those in ML CrI_3. The higher-frequency edge states (blue line) are composed of only edge Cr atoms represented by the blue spheres in Fig. 10(a), while the lower-frequency states (red line) are composed of only those at the opposite edge, and hence the chirality in these edge states is lost. Although the chirality of the magnon edge states is lost, the edge states satisfy broken time-reversal symmetry relation ($\omega_{\mathbf{k}} \neq \omega_{-\mathbf{k}}$) as a result of enhanced second-nearest-neighbor DMIs, $D^{\parallel}_{(2)}$, that connect the two second-nearest-neighboring Cr atoms at the one edge of the nanoribbon. The broken time-reversal symmetry properties of the magnon edge states manifest in different

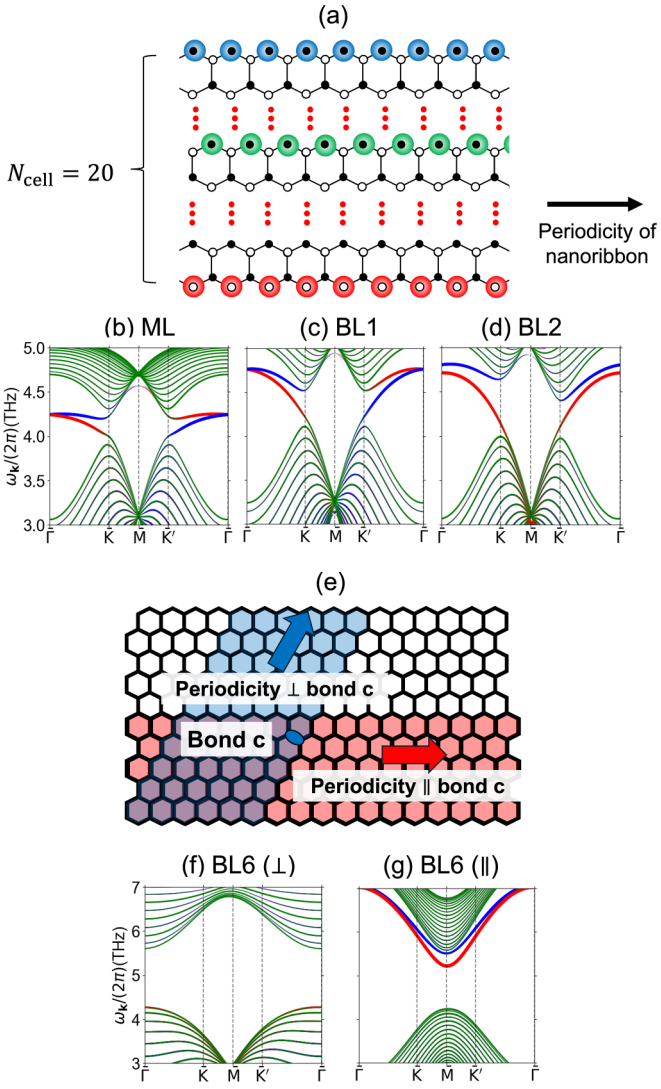

FIG. 10. (a) Quasi-one-dimensional (1D) nanoribbon geometry with zig-zag termination and width of 20 unit cells of honeycomb lattice. Two Cr atoms at the opposite edges are represented by blue and red spheres, while a Cr atom at the middle of the nanoribbon is represented by green spheres. White and black spheres represent two symmetrically distinct Cr atoms in the 2D unit cell. Magnon dispersion of (b) ML CrI_3, bilayer CrI_3/As (c) BL1, and (d) BL2. (e) Two different nanoribbon geometries can be made for BL6 stacking orders, where periodicity is perpendicular or parallel to the first-nearest-neighbor bond c (the significantly enhanced $J^{ex}_{(1),c}$) as indicated by blue and red arrows, respectively. Magnon dispersion of the BL6 stacking order, where periodicity is (f) perpendicular and (g) parallel to the bond c. In (b), (c), (d), (f), and (g), red, green, and blue lines correspond to the contribution of the Cr atom indicated by red, green, and blue spheres in (a), respectively, to magnon dispersion [59].

magnon occupation numbers and magnon group velocities between two counterpropagating magnons at one edge.

We note that the closing of the gapped bulk states by two localized edge states in the magnon dispersion of 1D nanoribbon BL2 and the **k** dependence of the localized edge states are attributed to accidental origins rather than the symmetry origins at the edges of the nanoribbons. Particularly, we compared the magnon dispersion of 1D nanoribbon BL2 with that of $CrI_3/MoTe_2$ and CrI_3/HfS_2 in Ref. [57], where the 2D space group is identical to that of BL2. In the Ref. [57], the broken vertical mirror symmetry between two Cr sublattices in the unit cell of the $CrI_3/MoTe_2$ and CrI_3/HfS_2 enters the magnon Hamiltonian via two distinct single-ion anisotropy (SIA) terms, which results in the two opposite nanoribbon edges being composed of Cr atoms with distinct SIA terms. Consequently, the opening of the bulk gap with flat edge states connecting the valley at $\bar{\mathbf{K}}$ and $\bar{\mathbf{K}}'$ is observed in the magnon dispersion of 1D nanoribbon $CrI_3/MoTe_2$ and CrI_3/HfS_2. In contrast, the broken vertical mirror symmetry in the BL2 in the present work enters the magnon Hamiltonian via second-nearest-neighbor spin-exchange interactions being distinct in magnitudes at two opposite edges of the nanoribbons, which gives rise to the **k** dependence of magnon edge states. The details of the second-nearest-neighbor spin-exchange interactions in BL2 are given in the Supplemental Material [35].

In the BL6 stacking order, two possible nanoribbon geometries can be made due to the broken rotational symmetry, as shown in Fig. 10(e). Taking the first-nearest-neighbor bond c, with $J^{ex}_{(1),c}$ being significantly enhanced, as the reference direction, one possible geometry has periodicity completely perpendicular to the bond c, while another possible geometry has periodicity parallel to the bond c. In the case of geometry with periodicity perpendicular to the bond c, labeled as BL6(⊥), we observed gapped magnon dispersion without localized edge states, with magnon frequency minimum and maximum around 4.5 and 5.0 THz at $\bar{\Gamma}$, as shown in Fig. 10(f). At these minimum and maximum, the two magnon states are composed of both edge Cr atoms and Cr atoms inside the nanoribbon. The reason for the unobserved localized edge states in Fig. 10(f) is due to the $J^{ex}_{(1),c}$ connecting the edge Cr atoms to those inside the nanoribbon, and this results in magnetic coupling between edge Cr atoms and those inside the nanoribbon being stronger than the coupling among edge Cr atoms that supports localized edge states. On the other hand, localized edge states exist in the magnon dispersion of the nanoribbon with periodicity parallel to the bond c, labeled as BL6(∥) [Fig. 10(g)], which is due to the relative orientation between periodicity and $J^{ex}_{(1),c}$ that supports the localized edge states propagation. The chirality of the localized edge states is also lost in the BL6(∥) due to the two Cr atoms at the opposite edges of the nanoribbons being symmetrically disconnected from each other due to broken vertical mirror symmetry, similar to the BL2 case. Additionally, the degeneracy between magnon states at the $\bar{\mathbf{M}}$, including the localized edge states, is lifted due to the broken threefold rotational symmetry. Specifically, all magnon states at six equivalent $\mathbf{M}'$s in 2D BZ of BL6 are no longer symmetrically connected by both threefold rotational and vertical mirror symmetry, which results in the magnon states at these $\mathbf{M}'$s having different magnon frequencies. In the quasi-1D nanoribbon geometry, these magnon states are zone folded and stacked together at the $\bar{\mathbf{M}}$ in 1D BZ, resulting in the nondegenerate feature shown in the Fig. 10(g).

Finally, we briefly discuss about the effect of the As monolayer on magnon relaxation in the CrI_3. Due to the electrically insulating properties, multimagnon interactions are assumed to be the main magnon relaxation channel in the present systems. The atomically thin 2D structure and pristine

surface/interface between the CrI_3 and As monolayer confine the magnon to propagate only along in-plane directions and suppress the two-magnon interactions-induced magnon relaxation. Therefore, the dominant magnon relaxation channel arises from three-magnon interactions, which also drives spontaneous magnon relaxation at zero temperature where no magnons are thermally excited [46,54].

Three-magnon interactions-induced magnon relaxation in collinear magnets is mainly determined by two factors: (i) the strength of magnetic interactions that couple the longitudinal (conserved) and transversal (oscillating) component of magnetic moments, e.g., $D_{ij}^{\perp}$, and (ii) the kinematic conditions, i.e., the splitting of single-magnon states into two-magnon states under energy and momentum conservation [54]. For the former factor, the $D_{ij}^{\perp}$ of CrI_3/As bilayers are generally larger than those of ML CrI_3 (see Fig. 6), which implies that stronger magnon relaxation might occur in the bilayer systems. On the other hand, for the latter factor, the increase of magnon frequencies in the bilayer systems results in the two-magnon continuum of the bilayer system residing in higher frequencies than that of ML CrI_3, which separates single-magnon states (magnon dispersion) and two-magnon continuum [46]. The separation between the single-magnon states and two-magnon continuum in the bilayer system decreases the available magnon decay channel and hence weakens the magnon relaxation. The competition between the two factors calls for additional investigation on the magnon relaxation in the CrI_3/semimetal bilayers.

IV. SUMMARY

In summary, we theoretically demonstrated symmetry-breaking-dependent modulations of isotropic spin-exchange interactions, Dzyaloshinskii-Moriya interactions, and topological magnons in CrI_3/As bilayers by employing the magnetic force theorem in first-principles calculations and linear spin-wave theory. In terms of spin-exchange interactions, the addition of As monolayer breaks the degeneracy of t_{2g} and e_g states in Cr d orbitals, in which the splitting between e_g states near the Fermi level gives rise to a first-nearest-neighbor spin-exchange constant being significantly enhanced by around two times from that of ML CrI_3. The addition of the As monolayer induces interfacial charge transfers to the I atoms, which breaks inversion symmetry in first- and second-nearest-neighboring Cr atoms. This process allows finite first-nearest-neighbor DMIs to appear and the second-nearest-neighbor DMIs to enhance. Furthermore, magnon dispersion gaps are opened at the edge of the BZ due to the second-nearest-neighbor DMIs, and the rotational symmetry breaking shifts the dispersion magnon gap from the corner of the BZ to the edge-side center of the BZ. We also confirmed the topological magnon phases from the existence of localized magnon edge states in the magnon dispersion of quasi-1D nanoribbon geometry. In particular, in stacking order with broken rotation symmetry, the existence of localized magnon edge states is controlled by the direction of nanoribbon periodicity relative to the crystallographic directions, particularly the direction of significantly enhanced first-nearest-neighbor spin-exchange interactions.

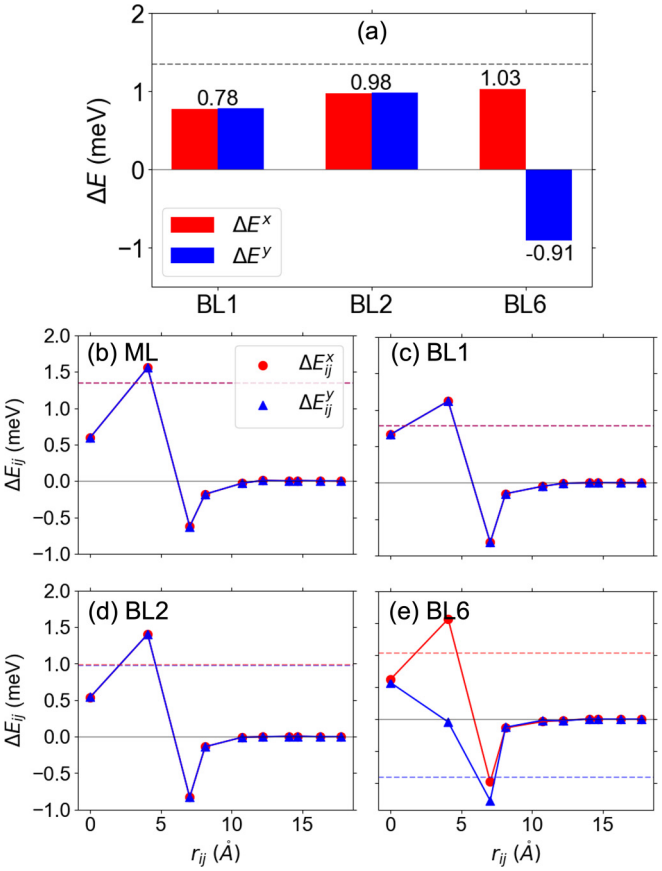

FIG. 11. (a) The magnetic anisotropy energy from the anisotropic spin-exchange constants, ΔE, of three stacking orders BL1, BL2, and BL6 in meV, and the dashed line represents ΔE of the monolayer CrI_3. The ΔE^x and ΔE^y are represented by red and blue bars, respectively. Contribution of Cr-Cr interaction separated by distance r_{ij} to the magnetic anisotropy energy, ΔE_{ij}^x and ΔE_{ij}^y, for (b) ML, (c) BL1, (d) BL2, and (e) BL6. In (b)–(e), Red circles and blue triangles represent the magnetic anisotropy energy contribution from the Cr-Cr pair, ΔE_{ij}^x and ΔE_{ij}^y, respectively. Red and blue dashed lines correspond to the total magnetic anisotropy energy, ΔE^x and ΔE^y, which is obtained by summing contributions from all Cr-Cr pairs [59].

ACKNOWLEDGMENTS

This work is partly supported by JSPS KAKENHI (Grants No. 23H00176 and No. 25K07225), Center for Spintronics Research Network, Osaka University. Numerical calculations were performed using computational facilities at Research Institute for Information Technology, Kyushu University, and the Supercomputer Center, the Institute for Solid State Physics, the University of Tokyo.

DATA AVAILABILITY

The data that support the findings of this article are openly available [59].

APPENDIX A: SPACE GROUP AND POINT GROUP SYMMETRIES OF SIX STACKING ORDERS

The presence of additional triangular lattice As monolayer below the CrI_3 changes the 2D space group of the unit cell and the point group of Cr atoms within the unit cell, which depends on the stacking order and the distance between As atom and the closest I atom. The 2D space group of the unit cell and the point group of the Cr atoms in six stacking orders are shown in the Table III. The point group of the Cr atoms determines the energy splitting of the d orbitals, which then affects the spin-exchange constants.

APPENDIX B: MAGNETIC ANISOTROPY ENERGY AND MAGNETIC EASY AXIS

Using the anisotropic spin-exchange constants, we calculated the magnetic anisotropy energies, which are given by,

$$\Delta E^x = E(90^\circ, 0^\circ) - E(0^\circ, 0^\circ),$$
$$\Delta E^y = E(90^\circ, 90^\circ) - E(0^\circ, 0^\circ),$$
$$E(\theta, \phi) = \frac{1}{2} \sum_{\alpha,\beta\in\{x,y,z\}} \sum_{i,j} J_{ij}^{\alpha\beta} S_i^\alpha(\theta, \phi) S_j^\beta(\theta, \phi), \quad \text{(B1)}$$

where two in-plane directions, x and y, are indicated by Fig. 1, and the matrix element of $J_{ij}^{\alpha\beta}$ is given by Eq. (2). In Table I, we show the comparison of the magnetic anisotropy energy for a freestanding ML CrI_3 in the present work and other theoretical references based on four-state method, which gives a good agreement between them in terms of sign and magnitude, and confirms the out-of-plane magnetic easy axis. In the presence of the As monolayer, the magnetic anisotropy energies of the CrI_3 layer, ΔE^x and ΔE^y, undergo weakening depending on the symmetry of stacking orders, and are shown in Fig. 11(a). In particular, the ΔE^y in the broken rotational symmetry BL6 becomes negative, and the magnetic easy axis changes from the out-of-plane z direction into the in-plane y direction.

To elucidate the origin of the magnetic anisotropy energy in the ML and three bilayers, we plotted the contribution of spin-pair interaction separated by distance r_{ij} to the magnetic anisotropy, ΔE_{ij}, in Figs. 11(b)–11(e). At distance $r_{ij} = 0$, the ΔE_{ij} corresponds to the contribution from the single-ion anisotropy of the individual Cr atom, while at finite distance $r_{ij} \neq 0$, the ΔE_{ij} corresponds to the contribution of the I atoms that mediated the Cr-Cr pair.

In the ML, the first-nearest-neighbor Cr-Cr interactions dominantly give rise to the magnetic anisotropy energy, followed by the second-nearest-neighbor interactions and single-ion anisotropy of the Cr atom, as seen in Fig. 11(b). However, the second-nearest-neighbor interactions give rise to a negative contribution to the magnetic anisotropy energy, in contrast to the first-nearest-neighbor interactions and single-ion anisotropy. The large contribution of the first-nearest-neighbor interactions to the magnetic anisotropy energy is mainly attributed to the Kitaev interactions in the 90° superexchange hopping between the Cr-I-Cr, where the strong SOC effect of I p states creates different energy hopping costs between the Cr-Cr pairs, depending on the magnetic moment directions [20–22,58].

In the presence of the As monolayer, the change of magnetic anisotropy energy in bilayer from that in ML is mainly attributed to the first- and second-nearest-neighbor interactions contributions, while the single-ion anisotropy contribution is relatively unchanged in all stacking orders (∼0.5 meV), as seen in Figs. 11(c), 11(d), and 11(e) for the BL1, BL2, and BL6, respectively. The first-nearest-neighbor interactions contribution remains dominant in the BL1 and BL2 (above 1 meV), while the magnitude of the second-nearest-neighbor interactions contribution increases to nearly 1 meV, resulting in the reduced magnetic anisotropy energy from that of ML, as seen in Figs. 11(c) and 11(d). On the other hand, in the BL6, the increase of the second-nearest-neighbor interactions contributions (nearly 1 meV) and the decrease of the first-nearest-neighbor interactions contributions magnitude to nearly zero result in negative ΔE^y, as seen in Fig. 11(e), changing the magnetic easy axis into y direction.

[1] A. Barman, G. Gubbiotti, S. Ladak, A. O. Adeyeye, M. Krawczyk, J. Gräfe, C. Adelmann, S. Cotofana, A. Naeemi, V. I. Vasyuchka, B. Hillebrands, S. A. Nikitov, H. Yu, D. Grundler, A. V. Sadovnikov, A. A. Grachev, *et al.*, The 2021 magnonics roadmap, J. Phys. Condens. Matter **33**, 413001 (2021).

[2] M. Gibertini, M. Koperski, A. F. Morpurgo, and K. S. Novoselov, Magnetic 2D materials and heterostructures, Nat. Nanotechnol. **14**, 408 (2019).

[3] B. Huang, G. Clark, E. Navarro-Moratalla, D. R. Klein, R. Cheng4, K. L. Seyler, D. Zhong, E. Schmidgall, M. A. McGuire, D. H. Cobden, W. Yao, D. Xiao, P. Jarillo-Herrero, and X. Xu, Layer-dependent ferromagnetism in a van der Waals crystal down to the monolayer limit, Nature (London) **546**, 270 (2017).

[4] N. Samarth, Magnetism in flatland, Nature (London) **546**, 216 (2017).

[5] F. Xiao and Q. Tong, Tunable strong magnetic anisotropy in two-dimensional van der Waals antiferromagnets, Nano Lett. **22**, 3946 (2022).

[6] X. Zhang, L. Wang, H. Su, X. Xia, C. Liu, B. Lyu, J. Lin, M. Huang, Y. Cheng, J.-W. Mei, and J.-F. Dai, Strain tunability of perpendicular magnetic anisotropy in van der Waals ferromagnets VI_3, Nano Lett. **22**, 9891 (2022).

[7] L. Fu, X. Wang, and W. Mi, Tunable electronic structure and magnetic anisotropy of two dimensional Mn_2CFCl/MoSSe van der Waals heterostructures by electric field and biaxial strain, Appl. Surf. Sci. **566**, 150683 (2021).

[8] J. Cenker, S. Sivakumar, K. Xie, A. Miller, P. Thijssen, Z. Liu, A. Dismukes, J. Fonseca, E. Anderson, X. Zhu, X. Roy, D. Xiao, J.-H. Chu, T. Cao, and X. Xu, Reversible strain-induced magnetic phase transition in a van der Waals magnet, Nat. Nanotechnol. **17**, 256 (2022).

[9] X. J. Dong, J. Y. You, Z. Zhang, B. Gu, and G. Su, Great enhancement of Curie temperature and magnetic anisotropy in two-dimensional van der Waals magnetic semiconductor heterostructures, Phys. Rev. B **102**, 144443 (2020).

[10] L. Webster and J. A. Yan, Strain-tunable magnetic anisotropy in monolayer $CrCl_3$, $CrBr_3$, and CrI_3, Phys. Rev. B **98**, 144411 (2018).

[11] W. Chen, Z. Sun, Z. Wang, L. Gu, X. Xu, S. Wu, and C. Gao, Direct observation of van der Waals stacking–dependent interlayer magnetism, Science **366**, 983 (2019).

[12] G. Hu, Y. Zhu, J. Xiang, T.-Y. Yang, M. Huang, Z. Wang, Z. Wang, P. Liu, Y. Zhang, C. Feng, D. Hou, W. Zhu, M. Gu, C.-H. Hsu, F.-C. Chuang, Y. Lu, B. Xiang, and Y.-L. Chueh, Antisymmetric magnetoresistance in a van der Waals antiferromagnetic/ferromagnetic layered $MnPS_3/Fe_3GeTe_2$ stacking heterostructure, ACS Nano **14**, 12037 (2020).

[13] S. J. Kim, D. Choi, K.-W. Kim, K.-Y. Lee, D.-H. Kim, S. Hong, J. Suh, C. Lee, S. K. Kim, T.-E. Park, and H. C. Koo, Interface engineering of magnetic anisotropy in van der Waals ferromagnet-based heterostructures, ACS Nano **15**, 16395 (2021).

[14] S. Yang, X. Xu, B. Han, P. Gu, R. Guzman, Y. Song, Z. Lin, P. Gao, W. Zhou, J. Yang, Z. Chen, and Y. Ye, Controlling the 2D magnetism of $CrBr_3$ by van der Waals stacking engineering, J. Am. Chem. Soc. **145**, 28184 (2023).

[15] K. Huang, E. Schwartz, D.-F. Shao, A. A. Kovalev, and E. Y. Tsymbal, Magnetic antiskyrmions in two-dimensional van der Waals magnets engineered by layer stacking, Phys. Rev. B **109**, 024426 (2024).

[16] J. P. Oviedo, K. C. Santosh, N. Lu, J. Wang, K. Cho, R. M. Wallace, and M. J. Kim, *In situ* TEM characterization of shear-stress-induced interlayer sliding in the cross section view of molybdenum disulfide, ACS Nano **9**, 1543 (2014).

[17] E. J. Sie, C. M. Nyby, C. D. Pemmaraju, S. J. Park, X. Shen, J. Yang, M. C. Hoffmann, B. K. Ofori-Okai, R. Li, A. H. Reid, S. Weathersby, E. Mannebach, N. Finney, D. Rhodes, D. Chenet, A. Antony, L. Balicas, J. Hone, T. P. Devereaux, T. F. Heinz, *et al.*, An ultrafast symmetry switch in a Weyl semimetal, Nature (London) **565**, 61 (2019).

[18] P. K. Muscher, D. A. Rehn, A. Sood, K. Lim, D. Luo, X. Shen, M. Zajac, F. Lu, A. Mehta, Y. Li, X. Wang, E. J. Reed, W. C. Chueh, and A. M. Lindenberg, Highly efficient uniaxial in-plane stretching of a 2D material via ion insertion, Adv. Mater. **33**, 2101875 (2021).

[19] J. Cenker, B. Huang, N. Suri, P. Thijssen, A. Miller, T. Song, T. Taniguchi, K. Watanabe, M. A. McGuire, D. Xiao, and X. Xu, Direct observation of two-dimensional magnons in atomically thin CrI_3, Nat. Phys. **17**, 20 (2021).

[20] C. Xu, J. Feng, H. Xiang, and L. Bellaiche, Interplay between Kitaev interaction and single ion anisotropy in ferromagnetic CrI_3 and $CrGeTe_3$ monolayers, npj Comput. Mater. **4**, 57 (2018).

[21] D.-H. Kim, K. Kim, K.-T. Ko, J. H. Seo, J. S. Kim, T.-H. Jang, Y. Kim, J.-Y. Kim, S.-W. Cheong, and J.-H. Park, Giant magnetic anisotropy induced by ligand *LS* coupling in layered Cr compounds, Phys. Rev. Lett. **122**, 207201 (2019).

[22] P. P. Stavropoulos, X. Liu, and H. Y. Kee, Magnetic anisotropy in spin-3/2 with heavy ligand in honeycomb Mott insulators: Application to CrI_3, Phys. Rev. Res. **3**, 013216 (2021).

[23] L. Chen, J.-H. Chung, B. Gao, T. Chen, M. B. Stone, A. I. Kolesnikov, Q. Huang, and P. Dai, Topological spin excitations in honeycomb ferromagnet CrI_3, Phys. Rev. X **8**, 041028 (2018).

[24] L. Chen, J.-H. Chung, M. B. Stone, A. I. Kolesnikov, B. Winn, V. O. Garlea, D. L. Abernathy, B. Gao, M. Augustin, E. J. G. Santos, and P. Dai, Magnetic field effect on topological spin excitations in CrI_3, Phys. Rev. X **11**, 031047 (2021).

[25] L. C. Zhang, F. Zhu, D. Go, F. R. Lux, F. J. dos Santos, S. Lounis, Y. Su, S. Blügel, and Y. Mokrousov, Interplay of Dzyaloshinskii-Moriya and Kitaev interactions for magnonic properties of Heisenberg-Kitaev honeycomb ferromagnets, Phys. Rev. B **103**, 134414 (2021).

[26] D. An and S. K. Kim, Intrinsic Nernst effect of the magnon orbital moment in a honeycomb ferromagnet, Phys. Rev. B **111**, 104436 (2025).

[27] Y. Höpfner, I. Mertig, and R. R. Neumann, Sign changes in heat, spin, and orbital magnon transport coefficients in Kitaev ferromagnets, Phys. Rev. B **111**, 214404 (2025).

[28] F. Zhang, X. Li, Y. Wu, X. Wang, J. Zhao, and W. Gao, Strong Dzyaloshinskii-Moriya interaction in monolayer CrI_3 on metal substrates, Phys. Rev. B **106**, L100407 (2022).

[29] M. U. Rehman, X. Dong, T. Hou, Z. Li, S. Qi, and Z. Qiao, Quantum anomalous Hall effect by coupling heavy atomic layers with CrI_3, Phys. Rev. B **100**, 195422 (2019).

[30] K. Nakamura, T. Ito, A. J. Freeman, L. Zhong, and J. Fernandez De Castro, Enhancement of magnetocrystalline anisotropy in ferromagnetic Fe films by intra-atomic noncollinear magnetism, Phys. Rev. B **67**, 014420 (2003).

[31] J. J. Liao, Y.-Z. Nie, X.-G. Wang, Z. -Y. Luo, Q. -L. Xia, R. Xiong, and G.-H. Guo, Spin reorientation and Curie temperature promotion in CrI_3 - Bi van der Waals heterostructures, Phys. Rev. B **107**, 184403 (2023).

[32] S. L. Dudarev, G. A. Botton, S. Y. Savrasov, C. J. Humphreys, and A. P. Sutton, Electron-energy-loss spectra and the structural stability of nickel oxide: An LSDA U study, Phys. Rev. B **57**, 1505 (1998).

[33] T. Björkman, A. Gulans, A. V. Krasheninnikov, and R. M. Nieminen, van der Waals bonding in layered compounds from advanced density-functional first-principles calculations, Phys. Rev. Lett. **108**, 235502 (2012).

[34] N. Mounet, M. Gibertini, P. Schwaller, D. Campi, A. Merkys, A. Marrazzo, T. Sohier, I. E. Castelli, A. Cepellotti, G. Pizzi, and N. Marzari, Two-dimensional materials from high-throughput computational exfoliation of experimentally known compounds, Nat. Nanotechnol. **13**, 246 (2018).

[35] See Supplemental Material at http://link.aps.org/supplemental/10.1103/kd5v-grhn for the supporting discussion on charge densities, electronic states of Cr *d* orbitals under SOC corrections, and anisotropic spin-exchange interactions in detail, which includes Refs. [37–39,59].

[36] J. H. Jung, C. H. Park, and J. Ihm, A rigorous method of calculating exfoliation energies from first principles, Nano Lett. **18**, 2759 (2018).

[37] A. I. Liechtenstein, M. Katsnelson, V. Antropov, and V. Gubanov, Local spin density functional approach to the theory of exchange interactions in ferromagnetic metals and alloys, J. Magn. Magn. Mater. **67**, 65 (1987).

[38] X. Wan, Q. Yin, and S. Y. Savrasov, Calculation of magnetic exchange interactions in Mott-Hubbard systems, Phys. Rev. Lett. **97**, 266403 (2006).

[39] X. Wan, T. A. Maier, and S. Y. Savrasov, Calculated magnetic exchange interactions in high-temperature superconductors, Phys. Rev. B **79**, 155114 (2009).
[40] S. Toth and B. Lake, Linear spin wave theory for single-Q incommensurate magnetic structures, J. Phys. Condens. Matter **27**, 166002 (2015).
[41] T. Holstein and H. Primakoff, Field dependence of the intrinsic domain magnetization of a ferromagnet, Phys. Rev. **58**, 1098 (1940).
[42] J. H. P. Colpa, Diagonalization of the quadratic boson Hamiltonian, Physica A **93**, 327 (1978).
[43] N. Bogoliubov, On the theory of superfluidity, J. Phys (USSR) **11**, 23 (1947).
[44] C. Xu, J. Feng, S. Prokhorenko, Y. Nahas, H. Xiang, and L. Bellaiche, Topological spin textures in Janus monolayers of the chromium trihalides Cr(Bi, X)$_3$, Phys. Rev. B **101**, 060404(R) (2020).
[45] J. M. Luttinger, A Note on the ground state in antiferromagnetics, Phys. Rev. **81**, 1015 (1951).
[46] J. Habel, A. Mook, J. Wilisher, and J. Knolle, Breakdown of chiral edge modes in topological magnon insulators, Phys. Rev. B **109**, 024441 (2024).
[47] M. Soenen, C. Bacaksiz, R. M. Menezes, and M. V. Milošević, Stacking-dependent topological magnons in bilayer CrI_3, Phys. Rev. Mater. **7**, 024421 (2023).
[48] D. Šabani, C. Bacaksiz, and M. V. Milošević, *Ab initio* methodology for magnetic exchange parameters: Generic four-state energy mapping onto a Heisenberg spin Hamiltonian, Phys. Rev. B **102**, 014457 (2020).
[49] W. B. Zhang, Q. Qu, P. Zhua, and C.-H. Lam, Robust intrinsic ferromagnetism and half semiconductivity in stable two-dimensional single-layer chromium trihalides, J. Mater. Chem. C **3**, 12457 (2015).
[50] W. Jin, H. H. Kim, Z. Ye, S. Li, P. Rezaie, F. Diaz, S. Siddiq, E. Wauer, B. Yang, C. Li, S. Tian, K. Sun, H. Lei, A. W. Tsen, L. Zhao, and R. He, Raman fingerprint of two terahertz spin wave branches in a two-dimensional honeycomb Ising ferromagnet, Nat. Commun. **9**, 5122 (2018).
[51] P. W. Anderson, Antiferromagnetism, Theory of superexchange interaction, Phys. Rev. **79**, 350 (1950).
[52] J. Kanamori, Superexchange interaction and symmetry properties of electron orbitals, J. Phys. Chem. Solids **10**, 87 (1959).
[53] D. I. Khomskii, *Transition Metal Compounds* (Cambridge University Press, Cambridge, 2014).
[54] M. E. Zhitomirsky and A. L. Chernyshev, *Colloquium*: Spontaneous magnon decays, Rev. Mod. Phys. **85**, 219 (2013).
[55] T. Moriya, Anisotropic superexchange interaction and weak ferromagnetism, Phys. Rev. **120**, 91 (1960).
[56] A. Corticelli, R. Moessner, and P. A. McClarty, Spin-space groups and magnon band topology, Phys. Rev. B **105**, 064430 (2022).
[57] R. Hidalgo-Sacoto, R. I. Gonzalez, E. E. Vogel, S. Allende, J. D. Mella, C. Cardenas, R. E. Troncoso, and F. Munoz, Magnon valley Hall effect in CrI_3-based van der Waals heterostructures, Phys. Rev. B **101**, 205425 (2020).
[58] M. A. Mcguire. H. Dixit, V. R. Cooper, and B. C. Sales, Coupling of crystal structure and magnetism in the layered, ferromagnetic insulator CrI_3, Chem. Mater. **27**, 612 (2015).
[59] A. Gumarilang and K. Nakamura, Tailoring spin-exchange interactions and topological magnons in 2D ferromagnetic van der Waals CrI3/As bilayer via multiple stacking orders: A first-principles study, Zenodo (2025), https://doi.org/10.5281/zenodo.17983790.

Correction: The elements As and I were erroneously set as Bi in several locations throughout the paper and have been fixed.